

Recyclable self-secreting autonomous healing dielectrics for millisecond water quality sensing

Received: 25 October 2024

Accepted: 12 May 2025

Published online: 01 July 2025

Check for updates

Mengmeng Liu^{1,2,9}, Hongchen Guo^{1,2,9}, Yu Jun Tan^{1,2,3}, Kelu Yu^{1,2}, Qiye Guan⁴, Evgeny Zamburg⁵, Wen Cheng^{1,2}, Xinyu Wang^{1,2}, Lili Zhou¹, Haiming Chen¹, Yunxia Jin², Xu Cheng^{1,2}, Fang-Cheng Liang¹, Baoshan Tang⁵, Hashina Parveen Anwar Ali^{1,2}, Jingyi Yang^{1,2}, Chaobin He¹, Yongqing Cai⁴, Aaron Voon-Yew Thean⁵, Zhong Lin Wang^{6,7} & Benjamin C. K. Tee^{1,2,5,8}

Developing a sustainable, in-situ responsive sensing method for continuously monitoring water quality is crucial for water use and quality management globally. Conventional water quality monitoring sensors face challenges in achieving ultrafast response time and are non-recyclable. We present a self-assembly approach for a closed-loop recyclable, autonomous self-healing and transparent dielectric material with nanostructured amphiphobic surfaces (termed 'ReSURF'). Our approach uses tribo-negative small molecules that spontaneously secrete onto the surface of the fluorine dielectric matrix via biomimetic microphase separation within minutes. ReSURF devices achieve millisecond water quality sensing response time (~6 ms), high signal-to-noise ratio (~30.7 dB) and can withstand large mechanical deformations (>760%, maximum of 1000% strain). We show ReSURF can be readily closed-loop recycled for reuse, underscoring its versatility. We further demonstrated its use in a soft stretchable fish-like robot for real-time water contamination (including perfluorooctanoic acid, a member of per- and polyfluoroalkyl substances (PFAS) and oily pollutants) assessments.

Water quality greatly impacts food security, agriculture, industries and urbanization. 3 billion people globally are experiencing water insecurity risk due to a lack of water quality monitoring data¹. World Health Organization (WHO) suggested that operational water quality monitoring must be simple: rapid tests (e.g., onsite testing equipment) or online (continuous) monitoring instrumentation, so that corrective action can be taken promptly². Conventional ways of obtaining such data are off-site and institution-based, requiring sample transportation

and centralized laboratories. On-site real-time surveillance with networked electronic devices^{3–6} to monitor real-time transient water quality changes are limited by responsive water quality sensors. Thus, developing in-situ fast-response sensors⁷ will advance water quality management surveillance options.

Electrochemical sensors and optical sensors have been developed for water quality monitoring, but they are either lab-based or exhibit slow time response⁸. Biosensors with encapsulation can achieve in-situ

¹Department of Materials Science and Engineering (MSE), National University of Singapore, Singapore, Singapore. ²Institute for Health Innovation & Technology (iHealthtech), National University of Singapore, Singapore, Singapore. ³Department of Mechanical Engineering, College of Design and Engineering, National University of Singapore, Singapore, Singapore. ⁴Institute of Applied Physics and Materials Engineering, University of Macau, Taipa, Macau, China. ⁵Department of Electrical and Computer Engineering (ECE), National University of Singapore, Singapore, Singapore. ⁶Beijing Institute of Nanoenergy and Nanosystems, Chinese Academy of Sciences, Beijing, China. ⁷School of Materials Science and Engineering, Georgia Institute of Technology, Atlanta, USA. ⁸The N.1 Institute for Health, National University of Singapore, Singapore, Singapore. ⁹These authors contributed equally: Mengmeng Liu, Hongchen Guo.

e-mail: benjamin.tee@nus.edu.sg

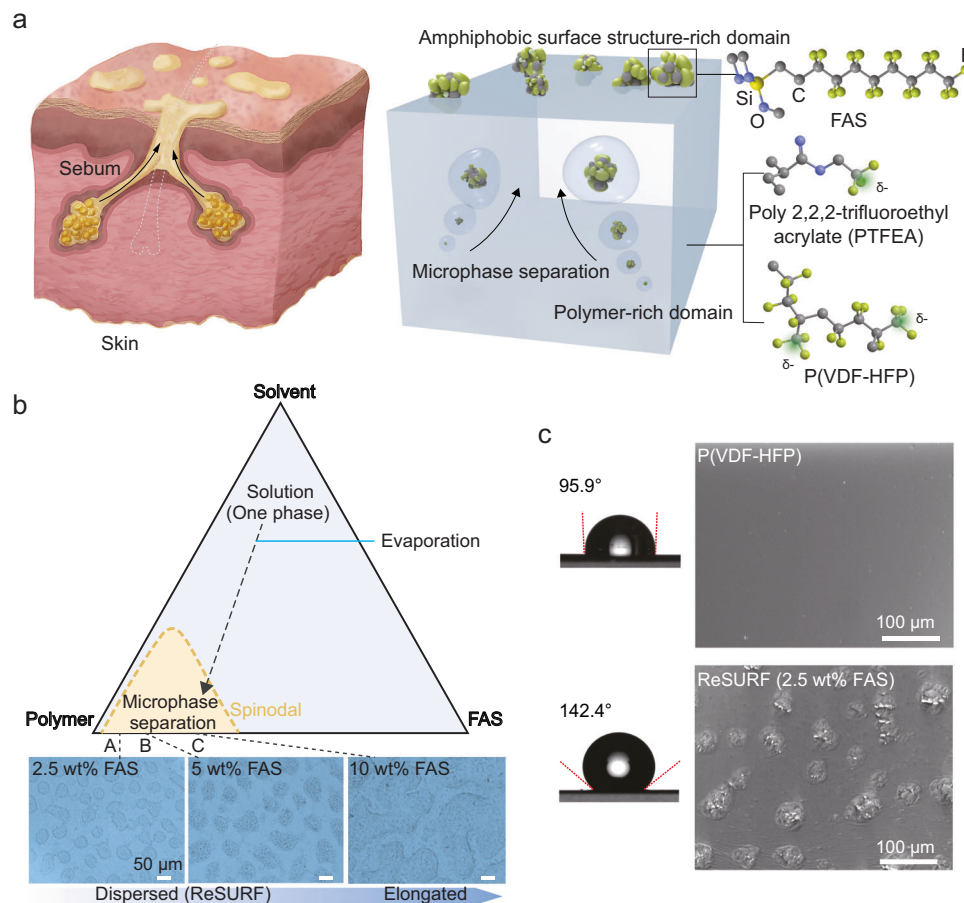


Fig. 1 | Concept and design of ReSURF by microphase separation. **a** Schematic illustration showing the fabrication of ReSURF. **b** Schematic illustration of a ternary phase diagram. Triggered by solvent evaporation, the system micro-separates into a 1H,1H,2H,2H-perfluorodecyltrimethoxysilane (FAS) surface structure-rich domain and a polymer-rich domain, with the surface microphases self-assembling into versatile and highly tunable morphologies. The FAS surface microphase substantially increases surface roughness and hydrophobicity, while the underlying

polymer matrix endows ReSURF with softness, stretchability, and a high κ . Both domains not only play distinct roles in this system but also synergize with each other to enhance device performance. **c** SEM images comparing the surface morphology of the 2.5 wt% FAS material with pure poly(vinylidene fluoride-co-hexafluoropropylene) (P(VDF-HFP)). The left image shows that the contact angle increases with the surface structure of FAS.

real-time water contamination detection, yet they have a similarly long response period of hours⁹. These slow responses were limited by the analyte mass transportation/reaction rate or the protein expression speed^{10,11}. Moreover, to achieve a high signal-to-noise ratio (SNR), sample pre-treatments or long incubation time (>0.5 hr) are required^{12,13}. The potential for recyclability was also not described in these devices.

To address these challenges, droplet-based triboelectric nanogenerators (TEGs) have potential for in-situ continuous monitoring. In such devices, TEGs generate transient peak signals based on rapid contact events and interfacial charge flows. This property has been explored for harvesting dynamic energies, real-time sensing and signaling^{14–18}. Recent breakthroughs in triboelectric technology enable its utilization for water quality improvement, achieving over 99.9999% bacteria and virus inactivation within a few minutes (<10 min) of walking¹⁹. When water droplets impact the hydrophobic TENG dielectric surface from a height, they will first spread and slip away. As they do so, the interfacial charge transportation and power generation occur within milliseconds²⁰. We can harness such ultrafast process to achieve continuous water quality (salinity) sensing when the target analytes contact the TENG dielectric surface due to the polarities of different ions or molecules²¹.

Possessing an amphiphobic surface is crucial for real-time water quality monitoring. Hydrophobic/superhydrophobic surfaces allow

continuous refreshment in contact with flowing water, thereby facilitating faster response times for continuous and rapid sensing and energy-harvesting. Water contaminations typically include both aqueous and organic phases (e.g., water pollution from oil spills), thus developing an amphiphobic and recyclable surface that allows for the timely shedding of liquid is desired.

Generating hydrophobic and amphiphobic surfaces are common strategies adopted by nature against water or oil ingressions. These are often generated through biological microstructures such as squama in butterfly wings or oily secretions such as sebum on human skins^{22–24} (Fig. 1a). Conventionally, oily secretions could be trapped within a porous matrix, but they do not automatically migrate to the surface.

Instead, we developed a ‘bottom-up’ self-assembly approach²⁵ within a non-porous soft composite material matrix that employs microphase separation to automatically initiate the secretion process. We termed this artificial closed-loop recyclable and self-healing composite material with amphiphobic surfaces for ultrafast water quality sensing as ‘ReSURF’.

ReSURF consists of microphase-separation of low-surface-energy fluorinated micro/nano-islands of 1H,1H,2H,2H-perfluorodecyltrimethoxysilane (FAS) self-secreted onto the outermost layer. The base polymer is made with poly(vinylidene fluoride-co-hexafluoropropylene) (P(VDF-HFP)) while the islands are made from fluorinated FAS. The microphase separation is rapid and occurs within 120 s. We

found that the FAS does not release into the surroundings due to the strong dipole interactions. Such a design increases the hydrophobicity without sacrificing its recyclability and healable attributes.

The ReSURF material can subsequently be used as a sensor device through the aforementioned droplet-based triboelectric effects. Compared to a pure P(VDF-HFP) droplet-based TENG device, our ReSURF-TENG devices (at 5 wt% FAS) showed a 330% improvement in output voltage performance, generating a high output voltage of 115.3 V and a current density of 17.6 mA m⁻².

The ReSURF low-surface-energy can shed water rapidly from the surface without the formation of liquid film, enabling sensor response in ~6 ms with a high SNR of 30.7 dB. We also found that the ReSURF-TENG devices exhibited repeatable, autonomous self-healing from physical and even laser damage (puncture/cutting) to their output generation and mechanical properties. We manifested a use case where ReSURF-TENG devices incorporated into soft robot fishes could submerge or float on the water surface frequently for in-situ water quality sensing.

Results

Design of ReSURF material and underlying mechanism

Pure P(VDF-HFP) is a hydrophobic polymer with high permittivity (κ) due to its high fluorine content. Poly(2,2,2-trifluoroethyl acrylate) (PTFEA) is also a fluorinated polymer with high self-healing properties. To increase surface roughness while reducing surface energy, we incorporated a small amount of fluorinated FAS into the fluoropolymer matrix (Methods). All the polymers contain CF₃ dipoles, maximizing dynamic dipole–dipole interactions for closed-loop recycling properties (Fig. 1a).

Unlike previous studies on microphase separation in infused materials or block copolymers (BCPs), most of which typically form porous internal structures, ReSURF introduces the concept of a biomimetic microphase separation surface (Fig. 1a). FAS is spontaneously secreted from within the material to the surface, where it self-assembles into a micro- to nanoscale low surface energy topography, representing an unexplored phenomenon.

We directly observed the surface microphase-separating process via optical microscopy (Supplementary Fig. 1, Supplementary Movie 1). Scanning electron microscopy (SEM) images at high-magnification and energy dispersive X-ray spectroscopy (EDS) elemental mapping further confirm the island-like FAS surface structure (Supplementary Fig. 2).

How could such distinct microphase separation occur even when both the polymer and FAS are fluorine-rich materials? Herein, we propose a mechanism for the fluorinated surface system. We schematically illustrated a ternary phase diagram (polymer, FAS and solvent) to show the evolution of surface structure formation (Fig. 1b). Microphase separation is triggered by solvent evaporation and ultimately forms polymer-rich domains and surface FAS-rich domains, driven by the minimization of surface energy (Fig. 1b and Supplementary Note 1; see density functional theory (DFT) calculations in Supplementary Fig. 39 and Supplementary Table 4).

Initially, FAS molecules aggregated into nanoscale aggregation and gradually grow over time (see dynamic light scattering (DLS) test in Supplementary Fig. 3). As solvent evaporation progresses, the concentrations of polymer and FAS gradually increase until a threshold is reached, resulting in a nonequilibrium state that causes the FAS to undergo microphase separation, effectively self-secreting onto the material surface²⁶. In striking contrast to previous classical processes, ReSURF microphase separation exhibits directional transport of FAS onto the surface rather than confinement within the interior (see cross-sectional SEM images in Supplementary Fig. 4 and X-ray micro-computed tomography (μ -CT) scan reconstructions in Supplementary Fig. 40 and 41). Once the

solvent has fully evaporated, solid islands with versatile morphologies rapidly self-assemble on the surface.

We observed that the surface microscopic morphology can be adjusted by varying the FAS concentration. The microphase-separation phenomenon is not obvious with the FAS concentration below 1 wt% (Supplementary Fig. 5). When the concentration of FAS increased to 2.5 wt% and 5 wt%, microphase separation occurs on the sample surface. The distributions of the microphase-separated structures indicate that the mean sizes of the micro/nanostructures at 2.5 wt% and 5 wt% FAS are ~50–70 μ m and 60–80 μ m, respectively, as shown in Supplementary Figs. 5 and 6.

At a higher FAS concentration of 10 wt%, the FAS microphases expand and elongate²⁷. Herein, the microscopic topography follows a well-defined trend: it can be tuned by FAS concentration. Upon reaching a concentration of 20 wt%, the FAS domains saturate and cover almost all surfaces.

Figure 1c shows the images of the surface micro/nanostructure of 2.5 wt% FAS ReSURF material compared with pure P(VDF-HFP). When the FAS concentration increases from 0 to 2.5 wt%, the contact angle increases from 95.9° to 142.4°. The increased hydrophobicity is attributed to the increase in roughness of low-surface-energy FAS islands.

Following Cassie-Baxter model²⁸, the hierarchical FAS structure leads to a trapped air layer with a reduction in the contact area with water, which improves its hydrophobicity, and the liquid-wetting state changes to the Cassie-Baxter state²⁹. After complete solvent evaporation, FAS molecules undergo polymerization to form solid islands, exhibiting an elastic modulus of ~102.20 MPa (Supplementary Fig. 7).

This composite surface can be applied to various substrates to form a hydrophobic layer (Supplementary Figs. 8, 9). In addition to plain substrates, ReSURF can also be applied to porous substrates to fabricate a superhydrophobic surface (contact angle: ~157.0°), as shown in Supplementary Fig. 10. Compared to previously reported combinations of P(VDF-HFP) and FAS for printing, electrospinning, or other hydrophobic materials, ReSURF demonstrates high hydrophobicity alongside recyclability, transparency, and self-healing properties (Supplementary Fig. 10, Supplementary Table 1). Moreover, the method is facile, tunable and does not require complex interfacial engineering.

ReSURF can be applied to a self-healing TENG device for ultrafast water quality monitoring and droplet energy harvesting. The design consists of three layers for the self-healable water-droplet sensor: a top self-healing ionogel electrode in contact with water droplets, a low-surface-energy dielectric for timely shedding of liquid and an ionogel back electrode (Supplementary Fig. 11). When the droplet impacts the amphiphobic surface, the interaction between the water and ReSURF induces a charged ReSURF-based capacitor; when the droplet slides down and contacts the top ionogel electrode, the ReSURF-based capacitor is discharged, and a voltage/current peak is generated (Supplementary Fig. 12).

Compared with conventional single-electrode devices, our device shows superior output (output voltage performance improved by 12.3 times)³⁰ and is comparable to state-of-the-art water droplet energy devices (Supplementary Table 2). This improved performance is attributed to the hierarchical fluorine-rich micro/nanostructured surface.

Surface potential and output performance of droplet-based ReSURF sensor

Atomic force microscopy (AFM) and Kelvin probe force microscopy (KPFM) were used to quantify the surface topography and surface potential difference (Fig. 2a, b). The microphase-separated FAS structures were further confirmed by the AFM phase images (Fig. 2b, c). The height of the 2.5 wt% FAS microstructure is around 300–500 nm, as shown in the AFM image (Supplementary Fig. 11). Each micro-island

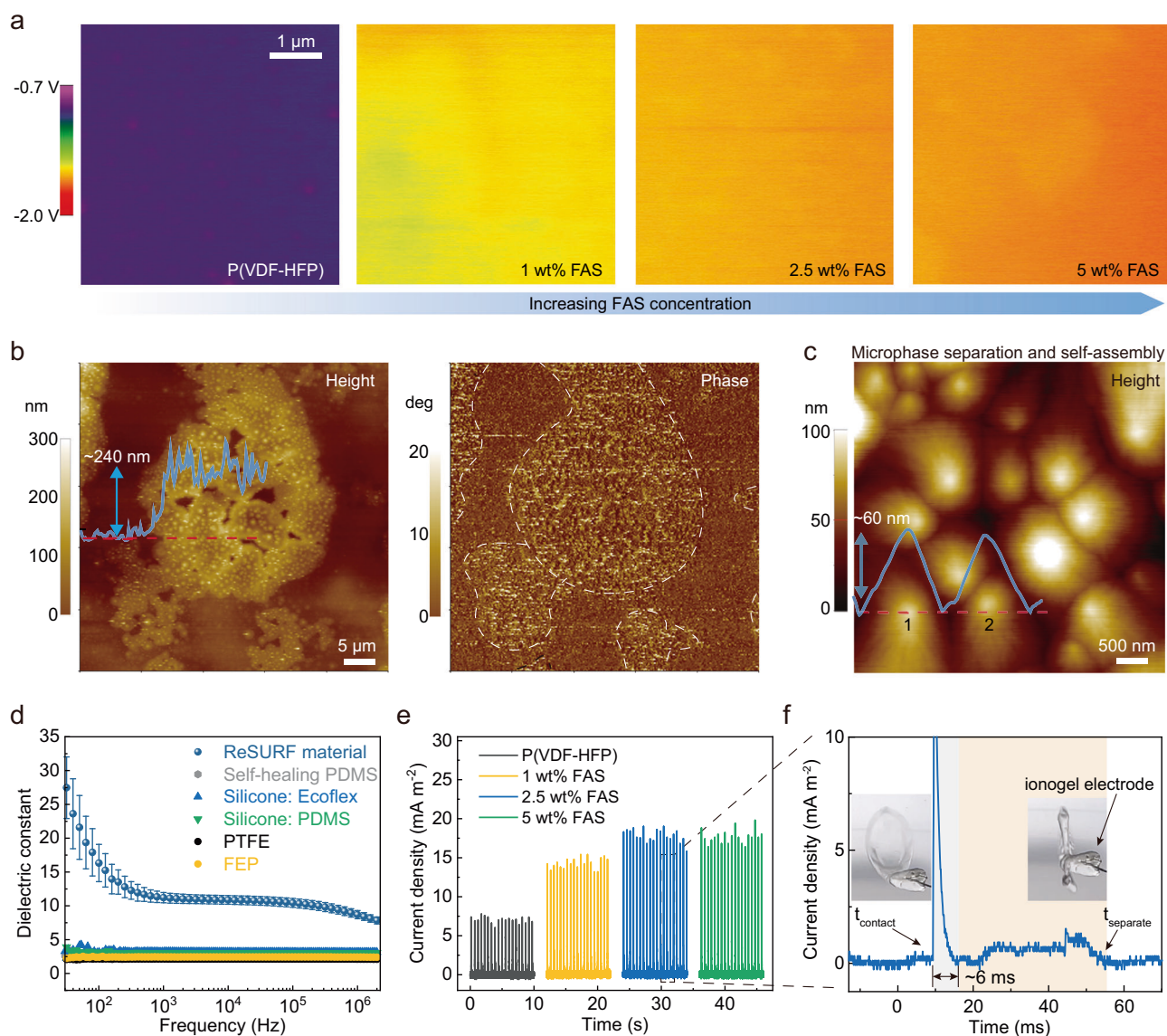


Fig. 2 | Characteristics of ReSURF and device output performance. **a** Kelvin probe force microscopy (KPFM) images of dielectric materials with different FAS concentrations. **b** The AFM topographic height profile and phase image corroborate microphase separation. **c** Zoomed-in AFM height images of the self-assembled nanoscale domains within an island-like structure (2.5 wt% FAS). **d** Comparison of the dielectric constants of ReSURF (2.5 wt% FAS) with those of fluorinated and other soft dielectric materials (PDMS: polydimethylsiloxane, PTFE: polytetrafluoroethylene, FEP: fluorinated ethylene propylene). Data are presented as mean

values and the error bars represent the standard deviation from three devices ($N = 3$). **e**, **f** Output current of the device with increasing the concentration of FAS. The inset of (**f**) illustrates the droplet contacting (left) and separating (right) from the ionogel electrode. t_{contact} and t_{separate} represent the moments when the water droplet first contacts and then separates from the top electrode, respectively. Output performance and response time measurements are obtained from flat devices on glass slides. The volume of each droplet is about $50.0 \mu\text{L}$. Height: $\sim 20 \text{ cm}$, Frequency: $\sim 2 \text{ Hz}$.

exhibits a hierarchical surface with nano-islands, significantly improving surface roughness and hydrophobicity (Fig. 2c, Supplementary Fig. 13). Increasing the FAS concentration to 5 wt% resulted in a greater structure height (1.2–1.8 μm), and the nanostructures tended to aggregate more closely (Supplementary Fig. 14).

To demonstrate whether the fluorinated FAS hydrophobic structure can lead to superior electrical performance, we compared the output performance of droplet-based pure P(VDF-HFP) and ReSURF-TENGs. As illustrated in Fig. 2e, f, when the FAS concentration increased from 0 to 5 wt%, the peak output voltage (current) increased from 34.7 V (7.0 mA m^{-2}) to 115.3 V (17.6 mA m^{-2}). The addition of a small amount of FAS, at 1 and 2.5 wt%, dramatically increased the output voltages by 2.9 and 3.3 times, respectively, compared to the pure P(VDF-HFP) device (Supplementary Fig. 15). Benefiting from the amphiphobic surface that allows for timely water droplet shedding,

the response time of the ReSURF sensor is $\sim 6 \text{ ms}$ (Fig. 2f, and Supplementary Fig. 16, Supplementary Movie 2), a one-order-of-magnitude improvement over state-of-the-art water quality sensors (Supplementary Table 3). The amphiphobic surface and fast response make ReSURF a promising candidate for in-situ water quality monitoring.

To gain further insight into the output performance improvement, KPFM was used to characterize the surface energy of the material. For the pristine P(VDF-HFP), the surface potential was calculated to be -0.97 V (Fig. 2a). The surface potential could be shifted to -1.64 V with the fluorinated FAS concentration increasing to 5 wt% (for 2.5 wt% FAS sample, -1.61 V), suggesting a more tribo-negative and stronger capability to attract and transfer electrons during the droplet spreading process than that of pure P(VDF-HFP) (Fig. 2a, Supplementary Fig. 17). The results were consistent with the output performance of the device at different FAS concentrations. With the fluorine-rich

main polymer and fluorinated FAS surface, the ReSURF material exhibits a lower surface potential than the commonly soft silicone materials³¹. Another reason for the performance improvement is the amphiphobic surface formed by the secretion of FAS. The hydrophobic hierarchical structure minimizes the water contact area, optimizing charge accumulation at the solid-liquid interface. Its 'lotus effect' promotes rapid liquid shedding and facilitates droplet detachment, ensuring a stable output (Supplementary Figs. 9–11). In addition, the ReSURF material exhibits a high dielectric constant (κ) value (Fig. 2d, ~3 times higher than that of common polytetrafluoroethylene (PTFE) and fluorinated ethylene propylene (FEP) dielectrics in the same frequency range), led to the superior output of the droplet-based TENG device due to high- κ charge capacity.

The output amplitude increases with the water dripping height (Supplementary Fig. 18, and Supplementary Figs. 42–44). Device performance with different setup geometries (tilt angle and ionogel volume) is shown in Supplementary Note 4. The transferred charges of the ReSURF-TENG (2.5 wt% FAS) were around 10.5 nC (Supplementary Fig. 19). By varying the external resistance, the maximum output areal

power density was measured to be -0.93 W m^{-2} at a matched resistance of about 430 k Ω (Supplementary Fig. 19b). We tested the droplet-based device for 2000 cycles, and the output voltage of the device showed almost no significant changes (Supplementary Fig. 19c).

Self-healing and closed-loop recyclability

The dynamic mechanical analysis (DMA) tests showed that the storage modulus of the dielectric material is higher than the loss modulus, indicating that the elastic component of the modulus dominates the viscous behavior (Supplementary Fig. 20a). ReSURF shows a low glass transition temperature (T_g) of $-24 \text{ }^\circ\text{C}$ (Supplementary Fig. 20b). FTIR spectra were used to compare ReSURF with different FAS concentrations (Supplementary Fig. 20c). The presence of FAS in the dielectric material can be identified from the strong characteristic peaks at 1145.6 cm^{-1} and 1198.6 cm^{-1} .

Figure 3a shows the microscopic images of the laser-scribed merlon pattern on the material. The laser tool was employed to induce controlled and repeatable damage, and at higher power settings, it resulted in carbonization. The scar gradually disappeared

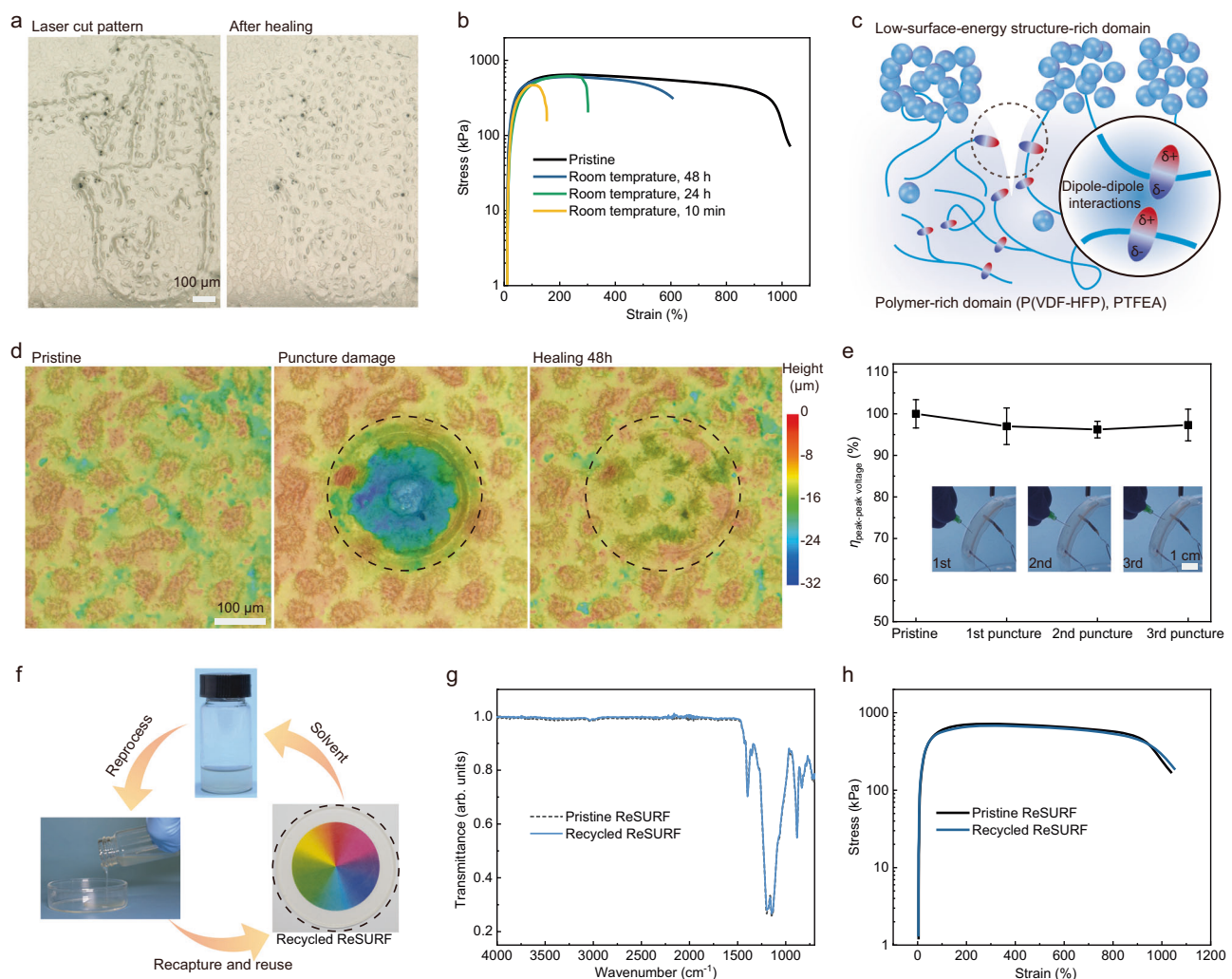


Fig. 3 | Self-healing properties and recyclability of the ReSURF material and device. **a** Photograph showing the laser-scratching material before and after healing (48 h, room temperature). **b** Stress-strain curves showing the ReSURF material healed after cut. **c** The schematic diagram of the self-healing mechanism of ReSURF: the dynamic dipole-dipole interactions (CF_3 , $\text{C}=\text{O}$, etc) within the polymer matrix, enable the material to exhibit self-healing properties. **d** 3D microscope images of devices after puncturing by needle (34 G). **e** Self-healing of the device with three subsequent punctures and healing under ambient environmental

conditions. The $\eta_{\text{peak-peak voltage}}$ changes can be attributed to the inevitable but slight change in dielectric thickness during damage and heal. The inset of **e** are photographs showing the devices punctured 3 times on a curved PDMS sphere. Data are presented as mean values and the error bars represent the standard deviation from three devices ($N=3$). **f** Photographs showing the closed-loop recyclability of ReSURF. **g** FTIR spectra showing the recyclability of the ReSURF material (5 wt% FAS). **h** Mechanical properties of the material after recycling (maximum of -1000% strain).

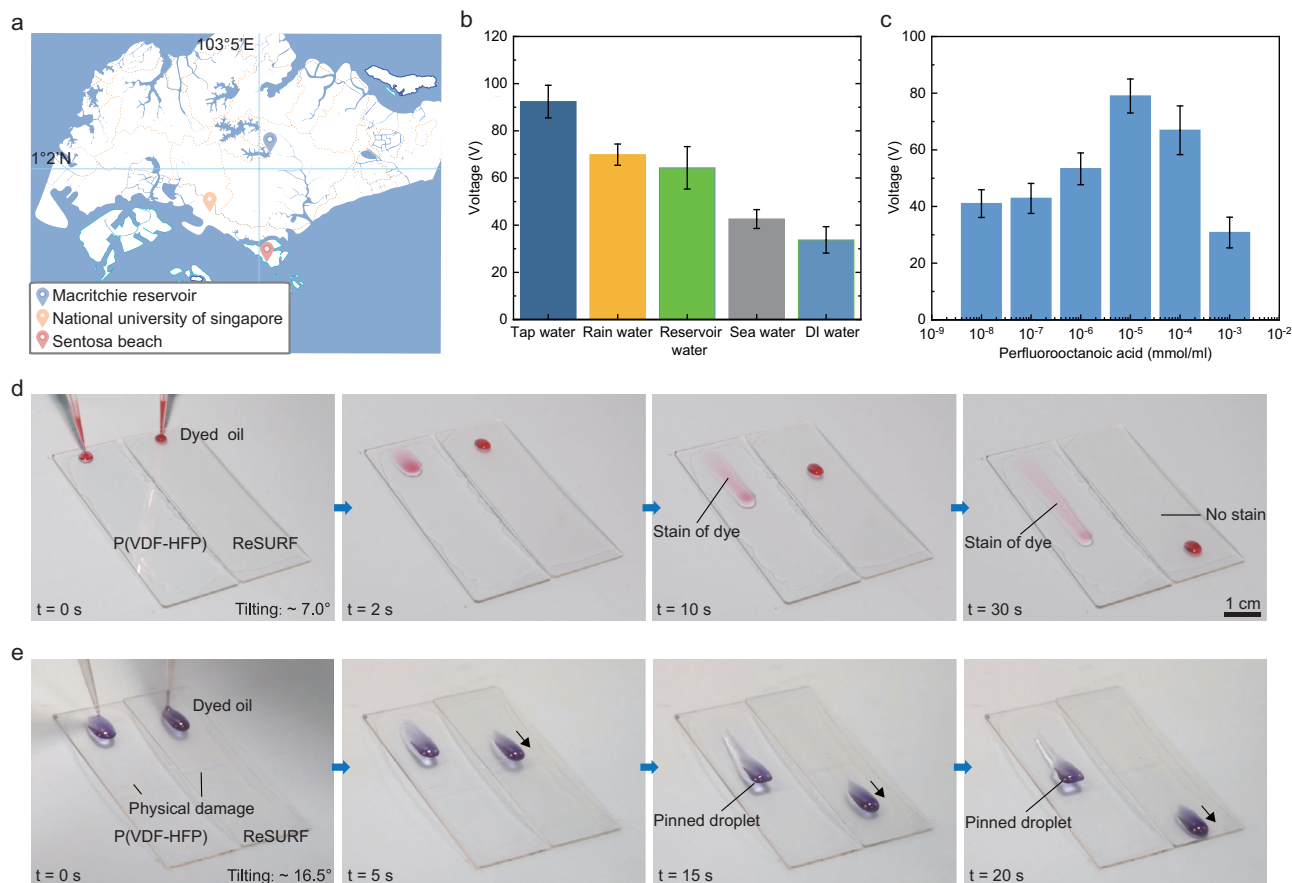


Fig. 4 | Water quality sensing and oil repelling performance. **a** Map of water sampling locations in Singapore. The map was generated using map data sourced from Singapore's National Water Agency, the Public Utilities Board (PUB). **b** Output voltage with various types of water sources (tap water, rainwater, reservoir water, seawater, deionized water) shows that different liquids generate distinct output signals with ultrafast response. Data are presented as mean values, and the error bars represent the standard deviation from three devices ($N = 3$). **c** Sensing of

polluted water with different perfluorooctanoic acid (PFOA) concentrations. Data are presented as mean values, and the error bars represent the standard deviation from three devices ($N = 3$). **d** Images comparing mobility of dyed oil droplets on ReSURF and pure P(VDF-HFP) flat surface (low viscosity oil, volume: $\sim 30 \mu\text{L}$). **e** Oil repellency of ReSURF after physical damage and healing (10 min healing at ambient), as compared to P(VDF-HFP) flat surface on which oil remains pinned at the damaged area (high viscosity oil, volume: $\sim 95 \mu\text{L}$).

over time at room temperature without any intervention (Supplementary Figs. 21, 22). The mechanical properties of the material recovered quickly after cutting. After 10 min of healing at room temperature, the ultimate tensile strength was restored to 73% of the pristine state, and the toughness increased with time (Fig. 3b). The high self-healing performance is attributed to the dipole-dipole interactions between the PVDF-HFP and PTFEA (Fig. 3c). In addition, the low T_g of ReSURF enhances the mobility of the polymer chains, thus facilitating its self-healing properties. The dielectric material and device can also self-heal after puncture (34 G needle) or plasma damage (Fig. 3d, and Supplementary Fig. 23). The soft device can work normally after healing with multiple punctures and cut damages (Fig. 3e, Supplementary Movie 3).

Thanks to its solubility in solvents and dynamic dipole-dipole interaction within the polymer matrix, the material can be readily recycled (Fig. 3f, and Supplementary Fig. 24, Supplementary Movie 4). Theoretically, such a simple closed-loop recycling strategy can endow ReSURF with an infinite lifecycle, potentially minimizing waste generation and environmental pollution. FTIR spectra of pristine and recycled ReSURF showed no significant chemical damage to the material (Fig. 3g). The stress-strain curves of the recycled material show excellent closed-loop recycling and reprocessing ability (maximum strain: $\sim 1000\%$, Fig. 3h). The recyclability aspect aligns with sustainable practices, reducing the need for virgin materials and promoting resource conservation.

For real-world applications, the primary challenge in recycling is the separation of different materials. The selective solubility of ReSURF in solvents such as acetone allows for effective separation from substrates like copper or silicon. Acetone dissolves the ReSURF material while leaving the substrate intact, facilitating separation through filtration.

Mobile, non-polymeric fluorocarbons are of increasing concern due to their potential environmental impact, particularly their high mobility. After complete phase separation, the FAS component undergoes polymerization, transforming into a solid-state material. This transformation enhances its stability and reduces its environmental mobility compared to free, non-polymeric fluorocarbons.

Water quality sensing and oil repelling

To investigate the performance of ReSURF under varying water conditions, we collected water samples from three distinct environments in Singapore: a coastal beach (Sentosa Beach), a freshwater reservoir (MacRitchie Reservoir), and rainwater (Fig. 4a). The device can be utilized to harvest hydrodynamic energy from tap water, raindrops, seawater and reservoir water (Fig. 4a, b). This device can be used as ultrafast sensor for detecting different perfluorooctanoic acid (PFOA) concentrations. The output voltage reaches a maximum value at $1 \times 10^{-5} \text{ mmol ml}^{-1}$ PFOA concentration with increasing salt concentration and then decreases (Fig. 4c). We attribute this increase of output voltage with higher concentration to the change of Debye length and

the decrease to the screening effect¹⁷. Notably, the sensor can detect PFOA concentration as low as 1×10^{-7} mmol ml⁻¹.

The device can work for detecting oil content in water. The output voltage decreases with the oil content increasing, and pure oil shows no output. This may be due to the non-polar/less polar nature of the oil decreasing the mixture polarity³². Therefore increasing the oil concentration in the mixture of water and oil may enhance the interaction with ReSURF material surface, thereby reducing the triboelectric charge density and generated output³³. Notably, the output voltage also shows a good linear relationship to the oil content on a logarithmic scale ($R^2 = 0.99$, Supplementary Fig. 25). While the voltage output variations indicate the presence of contaminants, PFOA and oil cannot be clearly separated based solely on these signals. Further refinement—such as integrating complementary sensing mechanisms—would be required to improve specificity for the precise identification of contaminants in future applications.

Benefiting from the FAS surface structure, the transparent surface exhibits high oil repellence. As shown in Fig. 4d, silicone oil is repelled on the ReSURF surface (rolling-off angle: $\sim 5.0^\circ$), but it wets, spreads out and stains the pure P(VDF-HFP) surface. The dielectric surface also serves as a self-healing coating to rapidly restore the oil-repellent function after cut damage (Fig. 4e, Supplementary Movie 5).

Stretchability and water soft robot application

The fully transparent droplet-based TENG device with ReSURF layer and ionogel electrodes is highly stretchable and flexible (Fig. 5a, Supplementary Fig. 26). The device can be twisted and stretched to 760% strain without any damage. On the contrary, replacing the ReSURF layer in the device with a polydimethylsiloxane (PDMS) layer as a dielectric layer breaks easily at a strain of 200% (Supplementary Fig. 27, Supplementary Movie 6). After releasing the strain, the device recovers to 177% of its original length due to the viscoelasticity of both the ionogel electrodes and the ReSURF layer (Supplementary Fig. 28). Notably, the FAS islands on the ReSURF surface are synchronously stretched with the ReSURF-TENG device without any detachments, indicating the firm bonding between the FAS phase and the fluorine-rich polymer phase (Fig. 5a bottom). This synchronous stretchability allows the device to be sensitive to strain. Figure 5b presents the voltage and current density outputs of the device when applying strain. The initial voltage and current density generated from a single tap water droplet are 30.40 V and $4.90 \text{ mA}\cdot\text{m}^{-2}$, respectively. The values drop to 20.75 V and $1.02 \text{ mA}\cdot\text{m}^{-2}$ when the device is strained to $\sim 300\%$ (Height: ~ 10 cm). This decrement attributes to the shrink of the effective contact area between the droplet spread and the FAS micro/nano-islands on the ReSURF surface (Supplementary Fig. 29). When a droplet impacts the stretched device, the droplet spread remains unchanged, however, the FAS micro/nano-islands within the spread are less as they are stretched to partially out of the spread range, leading to a decrease in the effective contact area and the accumulated charges. As a result, the output of the device decreases along with the increasing strain. Releasing the strain, the FAS micro/nano-islands return synchronously with the device, and the outputs are also restored (Supplementary Fig. 30, Supplementary Movie 7). Furthermore, the device output is slightly changed even after being immersed in DI water for 96 hrs and dried (Supplementary Fig. 31).

Next, we applied the ReSURF-TENG device for rapid in situ water quality monitoring and early warning of deviation from the water quality baseline. We developed a pufferfish-like underwater soft robot for in situ water quality monitoring (Supplementary Figs. 32, 33). Figures 5c, d depicts the sampling and assessment process of the lab-based pufferfish soft robot. The ReSURF-TENG device is stuck to the pufferfish belly by glue. A water inlet for sampling is fixed near the device with one end hanging over the top of the device while other end connects to a syringe pump with a check valve for water sample collection. An air inlet for inflating is also connected to the pufferfish

mouth with one end and the other end is linked to an air pump. In operation, the entire pufferfish soft robot sinks at the desired water-assessing spot first. Then the air is pumped into the pufferfish to inflate it; the fish starts soaring from the water bottom to the water surface due to the buoyant force and flipping, exposing the ReSURF-TENG device to the air. While the fish is floating on the water surface, the water sample is drawn by the syringe pump from the water body and dripped on the device. The sampling depth can be decided by the water tube length. Thus, the output spike signals are collected to assess the water quality and decide if it deviates from the water quality baseline (Supplementary Figs. 34, 35).

Figure 5d presents the real states of the lab-based pufferfish soft robot. Figure 5e reveals the real-time output signals from the ReSURF-TENG device on the pufferfish soft robot during the entire inflating-deflating-inflating process (Supplementary Movie 8). The initial signals are background noise (I) as the device electrodes are immersed in water. After inflation, the pufferfish rises from underwater and floats at the surface, exposing the electrodes to the air and reducing the background noise (II). Then the syringe starts drawing external water and dripping the droplets onto the devices. Thus, the stable output voltage signals are generated (III). Noted that the voltage signals are lower in the beginning as the first few drops accumulate fewer charges. Pumping out the air and the pufferfish deflates. The noisy signals start to appear as the water-dropping angle decreases (IV) till the electrodes are fully immersed again (V) (Supplementary Fig. 36). However, the signal can restore completely when the pufferfish is reinflated (VI).

This in situ pufferfish robot can be used for early alert of water quality change by distinguish the voltage signal change in amplitude from the water quality baseline. For example, Fig. 5f presents the signal baseline of DI water (~ 6 V), and this signal (~ 4 V) deviates from its baseline when the water contains 1 wt% of cooking oil pollutant. The ultrafast response time of our device enable a short sampling time of 10 s to collect stable signals, which is sufficient for early warning of the abnormal water quality change. This early alert monitoring function works on other water bodies and water pollutants (Supplementary Fig. 37).

Our pufferfish robots show potentials for real application scenarios due to its robustness and feasibility. First, the robot is robust as the ReSURF-TENG sensor is adhered to the silicone surface by silicone glue that is flexible and water-resistant. Second, the data collected from the sample can be easily transmitted by cables or wirelessly, as the pufferfish robot holds a sufficient space for placing a chip inside its body. Thirdly, since the air pressure and water sample volume required for operating the robot is small, low-power pumps will meet the requirements. Therefore, our pufferfish robots are suitable for deploying in confined space of modern industry and agriculture such as sewage treatment plant or rice paddy fields.

The response time and signal-to-noise ratio are summarized in Fig. 6 to compare with previously reported water quality sensors. Remarkably, our device exhibits signal-to-noise ratio up to 30.7 dB and fast response time (~ 6 ms), outperforming most existing bio-optical, bioelectronic, bioelectrochemical, electrochemical, chemo-optical and electronic sensors (Fig. 6, and Supplementary Table 3). The superior performance results from i) the amphiphobic surface (to shed water droplets in a timely); ii) hierarchical tribo-negative fluorine micro/nano islands (allowing for rapid charge transfer); iii) the high κ ReSURF induced by polarization of CF_3 groups. This reduced response time and high signal-to-noise ratio places our ReSURF in a previously unexplored area of performance for real-time water quality sensing (Fig. 6), and provides a solution to the previous limitation of response times in excess of minutes.

Discussion

Inspired by human skin's ability to use secreted sebum as an oily hydrophobic layer, we demonstrated a facile approach to fabricating

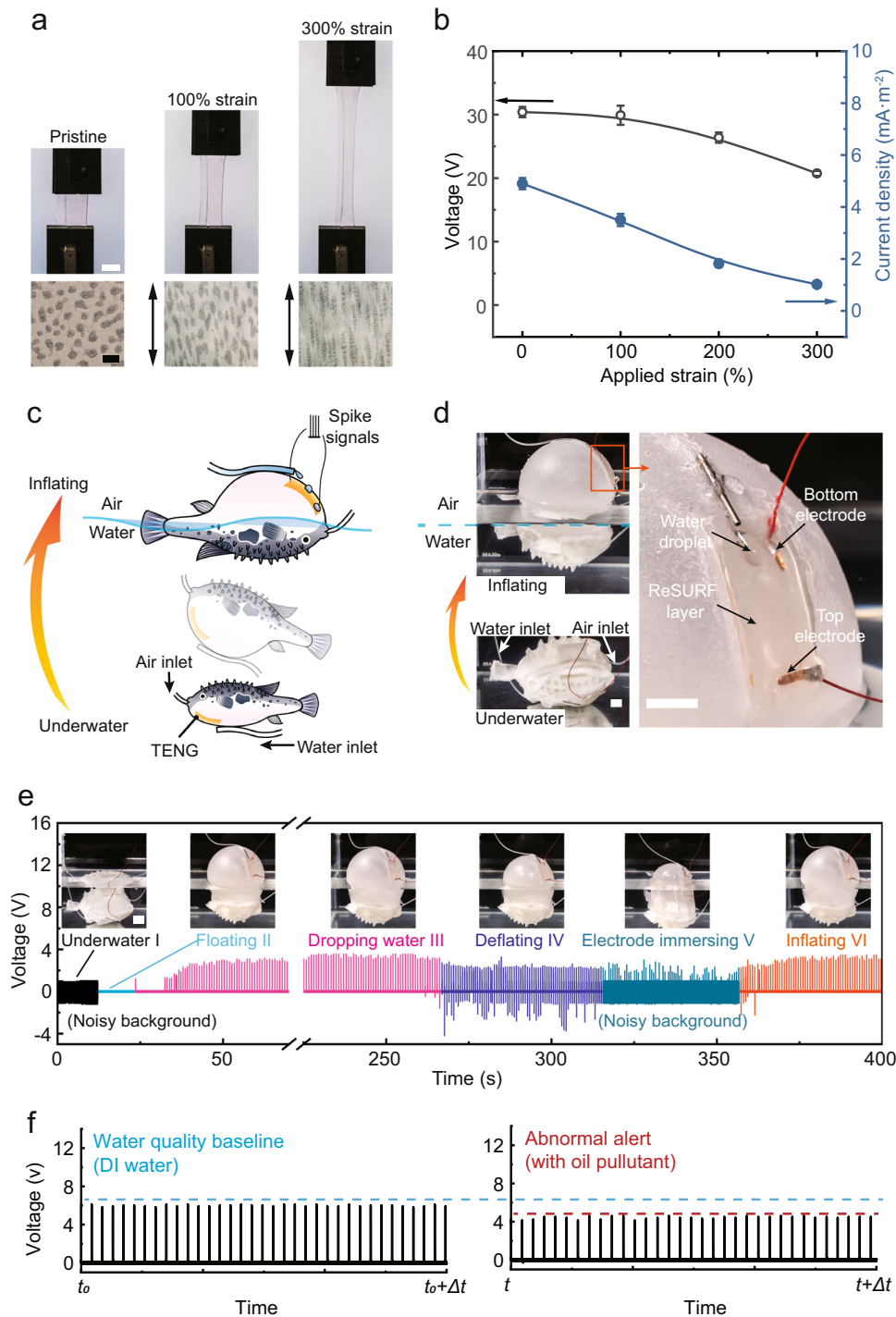


Fig. 5 | Stretchable droplet-based nanogenerator for underwater soft robot assessing water quality. **a** Photos (top) and optical microscopy images (bottom) of the fully transparent droplet-based nanogenerator straining from the pristine state (left) up to 100% (middle) and 300% (right). The black arrows at the bottom represent the strain directions. Scale bar: 1 cm (top) and 100 μm (bottom). **b** Voltage and current density outputs of the droplet-based nanogenerator changing with the applied strain. Data are presented as mean values and the error bars represent the standard deviation from three devices ($N = 3$). **c** Schematic of an underwater pufferfish-like soft robot attached with the droplet-based nanogenerator for water quality assessment. The pufferfish immersing in water is expanded and rises from the water bottom to the surface when being inflated (with air), exposing the nanogenerator to

the air for collecting the corresponding spike signals from the water droplets. **d** Photos of the underwater pufferfish soft robot rising from the bottom to the surface (left) and the attached droplet-based nanogenerator (right). Scale bar: 1 cm (both left and right). **e** Real-time voltage outputs of the droplet-based nanogenerator on the pufferfish soft robot during the entire inflating-deflating-inflating process (Supplementary Movie 8). I–VI represent different sessions and are denoted as (from left to right): I–Underwater, II–Floating, III–Dropping water, IV–Deflating, V–Electrode immersing, and VI–Inflating. Insets are the photos of each corresponding session. Scale bar: 2 cm. **f** The voltage outputs obtained from the same inflating pufferfish soft robot in **e** showing the water quality baseline of deionized (DI) water and the abnormal alert when the water contains 1 wt% oil pollutant.

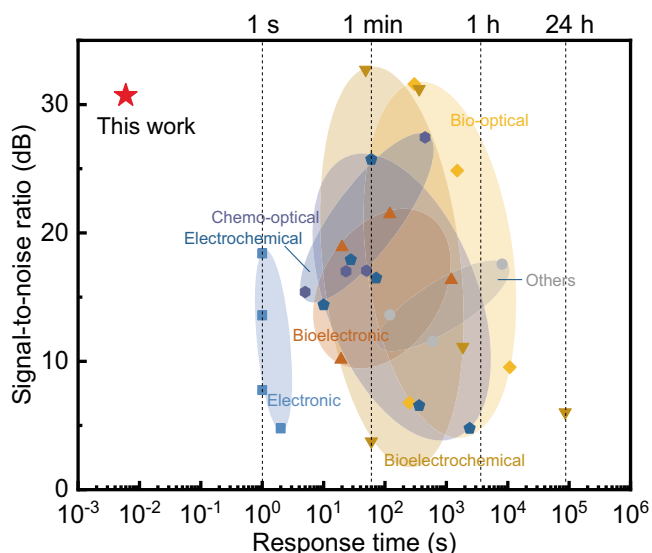


Fig. 6 | Response time comparison. Comparison of performances in this work and state-of-the-art water quality sensors, expressed in terms of the response time and signal-to-noise ratio. This provides a benchmark for water quality sensors.

hierarchical dielectric surfaces through microphase separation. Compared with pure P(VDF-HFP), the fluorinated surface micro/nanostructure improves the surface amphiphobic properties and output voltage/current density of the device without significantly sacrificing its recyclable and self-healing properties. The material can be fabricated as a freestanding dielectric layer or as a coating on a broad variety of substrates, such as a porous material, to form a superhydrophobic surface. To date, no reported material surfaces possess the properties of ReSURF: recyclable, self-healing, transparent, high κ , amphiphobic, low-surface-energy, and adjustable surface micro/nanostructure size/height in a single material system. The topology of ReSURF complex materials have the potential to inspire the development of synthetic mimics for applications in soft sensors, as well as optical and mechanical metamaterials. Future advancements in ReSURF may explore fluorine-free alternatives that comply with emerging regulations, ensuring its sustainability and continued applicability across various applications. We anticipate our ReSURF soft water quality sensing strategy will enable opportunities for sustainable applications in agriculture, recycling of urban water, electronic skins and soft robotics.

Methods

Materials

Poly(vinylidene fluoride-co-hexafluoropropylene) (PVDF-HFP, FC 2230, 3 M), 1H,1H,2H,2H-perfluorodecyltrimethoxysilane (FAS, 95%), 1-ethyl-3-methylimidazolium bis(trifluoromethylsulfonyl)imide (EMITFSI, 95%, Solvionic), and 2,2,2-trifluoroethyl acrylate (TFEA, 98.0%, TCI) were used as received. Urea (99%), trisodium phosphate (96%), potassium chloride (99%), calcium chloride (CaCl_2 , 96%), and silicone oil (10 cSt) were obtained from Sigma-Aldrich and also used as received. FAS should be stored in a dry box after use.

Fabrication of the ReSURF with amphiphobic surface

The ReSURF material was prepared by mixing 2 g of poly(vinylidene fluoride-co-hexafluoropropylene) (P(VDF-HFP), amorphous) with 2 wt % PTFEA (Supplementary Fig. 38), and varying concentrations of 1H,1H,2H,2H-perfluorodecyltrimethoxysilane (FAS, 0 wt%, 1 wt%, 2.5 wt %, 5 wt%) in 6 mL of acetone. The solution was stirred for at least 6 h to ensure a well-dispersed mixture. The solution was sonicated for 10 min to remove air bubbles, then cast into a glass petri dish with a glass

cover. The acetone evaporated to form a film, and the thickness of ReSURF could be adjusted by controlling the volume of the ReSURF solution (Supplementary Fig. 45).

Surfaces with FAS vapor deposition method (Supplementary Fig. 10b, c) were prepared as follows: 2 g of P(VDF-HFP) was dissolved in 6 mL of acetone and stirred for at least 6 h to obtain a well-dispersed solution. The solution was sonicated and then poured onto with a piece of glass slide for acetone evaporation. 30 wt% FAS dissolved in hexane and were placed into a glass container, and then the as-mentioned P(VDF-HFP) was upside down on the container and heated at 40 °C in a sealed oven for 90 min. A hydrophobic layer of FAS was formed via the vapor. FAS casting surfaces were prepared by direct drop-casting pure FAS on the P(VDF-HFP) surface.

Synthesis of PTFEA

PTFEA was synthesized by polymerizing 2,2,2-trifluoroethyl acrylate (TFEA) monomer. The ratio of TFEA (10 g) to initiator was maintained at 250:1, and the reaction was conducted at 82 °C under a nitrogen atmosphere for 8 h to initiate polymer chain growth. The resulting product was then dried in an oven at 70 °C for 1 h.

Fabrication of the droplet-based nanogenerator device

The droplet-based self-healing device was fabricated by sandwiching the ionogel electrode between ReSURF layers. Unless stated otherwise, we chose the 2.5 wt% FAS dielectric for the device based on the output and transparency performance. The size of the device is around 1.5 cm \times 3.5 cm \times 1 mm. A small piece of ionogel (-0.5 cm \times 1.5 mm \times 1 mm) was placed at the bottom of the device as the top electrode contacting with the spreading water droplet. The ionogel electrode was prepared by mixing 16 g of P(VDF-HFP) with 4.5 mL of 1-ethyl-3-methylimidazolium bis(trifluoromethylsulfonyl)imide (EMITFSI) in 40 mL of acetone³⁴. The tilt angle is fixed at 55° (Supplementary Fig. 43). Aluminum tape, Cu wire electrode was used to electrically connect the ionogel electrode for output testing. The Cu-based droplet-based nanogenerator device is prepared by ionogel on the surface of the ReSURF/Cu (Supplementary Fig. 8, Supplementary Fig. 31).

Device characterization

An oscilloscope (KEYSIGHT MSOX2024A) was used to test the output voltage signal of the droplet device. The output charge transfer quantity and the current of the device were obtained by Keithley 6514 electrometer and Stanford low-noise current preamplifier (SR570), respectively. The AFM measurements were carried out using Park Systems NX20. KPFM images with different FAS concentrations were scanned at a scan speed of 0.5 Hz in noncontact mode. A thin layer of Au (area: 1.2 mm \times 1.2 mm) sputtered on the surface works as a reference (Supplementary Fig. 17).

The surfaces were imaged by KEYENCE digital microscope (3D images) or SEM using a Zeiss sigma 300 with SmartEDS system. The measurements shown in Figs. 2d, 3e, 4b, c and 5b were performed on three independent devices (N=3) to assess reproducibility. FTIR measurements were performed by an FTIR Vertex 70 spectrometer from 500 to 4000 cm^{-1} . The mechanical property was obtained by Instron tensile testing systems (68SC-1). Contact angle and rolling-off angle were measured by goniometer rame-hart 290-u1, the rolling-off angle is -5.0° (silicone oil, 10 cSt). The dielectric constants were measured using the E4980A Precision LCR Meter. 3D X-ray micro-computed tomography (μ -CT) scan reconstructions were performed using a ZEISS Xradia 515 Versa X-ray microscope (Carl Zeiss). The sample was attached to the end of a -2 cm-long pin using a cyanoacrylate-based adhesive and mounted onto a ZEISS specimen holder for scanning. 3D reconstruction and visualization were conducted using TXM3DViewer. Dynamic light scattering (DLS) measurement was performed by Malvern Zetasizer Pro (Supplementary Fig. 3b). 5 wt% FAS was mixed with acetone, and after stirring (10 min),

then DLS was employed to assess the variation in aggregation size (20–260 min). Throughout the DLS testing, the solution remained sealed within the quartz cell, with no acetone undergoing evaporation. To minimize the impact of P(VDF-HFP) polymer chains on the FAS nanoscale aggregation size measurement, no P(VDF-HFP) was added to the test solution. Thus, the measured aggregation sizes exclusively represent those of FAS.

The self-healing PDMS (Fig. 2d) for dielectric constant test was prepared by mixing bis(3-aminopropyl) terminated poly(dimethylsiloxane) ($\text{H}_2\text{N-PDMS-NH}_2$), bis(hydroxyalkyl) terminated poly(dimethylsiloxane) (HO-PDMS-OH) and the 4,4'-Methylenebis(cyclohexyl isocyanate) (coupling agent).

Water quality sensing

The rain water is collected from rain droplets in Singapore. The solution for oil sensing is prepared by mixing cooking oil (plant oil: sunflower oil) with different volumes into deionized water in a vortex mixer. The dyed oils in Fig. 4d is prepared by mixing silicon oil (10 cSt) with Sudan red while 4e is plant oil (sunflower oil) with Solvent blue. The polluted water was prepared by mixing for 0.5 g urea, trisodium phosphate, 5 g potassium chloride and 0.01 g calcium chloride in 200 mL deionized water for N, P, K and Ca elements. The volume of each droplet is around 50 μL . The droplet channel width and the use of a syringe pump for consistent droplet volume and speed have been considered to minimize measurement variability. A filter is used to remove contaminants larger than the droplet channel width.

Pufferfish soft robot

The pufferfish-like underwater soft robot consists of four parts: i) the elastic skin, ii) the skeleton, iii) the balance, and iv) the elastic belly. The elastic skin and the belly are fabricated by casting the silicone-based elastomer on the mode surface and peeling it off (Supplementary Figs. 32, 33). To be more specific, the silicone-based elastomer is prepared by mixing Ecoflex 00-30 and 15 wt% cellulose fibers using the SpeedMixer. The mixture is then poured on the 3D-printed pufferfish body mold or the glass sphere mold and cured at 70 °C for 30 min. After curing, the skin and the belly are peeled off for assembling. Two half-oval skeletons are 3D printed and glued to each other with a sand balance covered inside. Then the cured pufferfish skin and belly are stuck to the skeleton and sealed by Silpoxy. The ReSURF-TENG device and the water inlet are also fixed on the outside of the belly with Silpoxy. To keep a consistent dripping water droplet size, the water inlet was a silicone tube with the end connected to a stainless steel 18 G nozzle. An air inlet silicone tube is inserted into the inside of the pufferfish and firmly fixed.

Lab-based water quality assessment demonstration

The pufferfish soft robot is immersed in a tank filled with water for water quality assessment. The water and air inlets are connected to a syringe and an air pump, respectively. A syringe pump is used to draw water from the tank and pump the water droplets to the ReSURF-TENG device. Noted that the syringe we used here connects to a check valve to prevent the water from flowing back to the tank when the syringe pump is pumping. To prevent the water inlet clogging from the oversized impurity, a filter can also be used before the water sample dripping to the TENG device. Then The signals from the TENG device are collected through the Picoscope. To assess different water qualities, we fill the tank with different water sources using the same pufferfish soft robot.

Calculation of conversion efficiency

We calculated the instantaneous conversion efficiency of the device, η , as follows:

$$\eta = \frac{\int_{t_{\text{contact}}}^{t_{\text{separate}}} U I dt}{mgh} \quad (1)$$

Where m is the droplet mass (0.05 g); g is the gravitational acceleration (9.8 m s^{-2}); the height (h) between the droplet and the device is about 0–20 cm; U is the output voltage; I is the output current; and t_{contact} and t_{separate} represent the moments when the water droplet first contacts and then separates from the top electrode, respectively. For our device, the mechanical energy of the impinging droplet ($\sim 50 \mu\text{L}$, height: 20 cm) is roughly $9.8 \times 10^{-5} \text{ J}$, and the conversion efficiency (η) is calculated to be about 2.4%.

Calculation of signal-to-noise ratio (SNR)

We calculated the SNR as follows:

$$\text{SNR}_{\text{dB}} = 10 \lg \left[\left(\frac{A_{\text{signal}}}{A_{\text{noise}}} \right)^2 \right] \quad (2)$$

Where A_{signal} is the amplitude of the signal and A_{noise} is the amplitude of the background noise. The current density was used for the SNR calculation. The setup geometry is as follows: droplet volume $\sim 50.0 \mu\text{L}$, height 20 cm, frequency 2 Hz, and tilt angle $\sim 55^\circ$.

DFT calculations

First-principles calculations were conducted utilizing the Vienna ab initio simulation package (VASP). To capture the weak van der Waals (vdW) interactions between polymers, the DFT-D3 functional augmented with Grimme correction was employed³⁵. The strength of interaction, crucial in understanding polymer-polymer interactions, was evaluated through the computation of the binding energy (E_b), employing atomic models with periodic boundary conditions. To prevent interference from periodic images, a vacuum region of $> 10 \text{ \AA}$ thickness was established. Brillouin zone sampling was achieved utilizing a Γ point, while the exchange-correlation energy was computed using the generalized gradient approximation (GGA) within the Perdew-Burke-Ernzerhof (PBE) framework. All calculations were conducted with an energy cutoff of 400 eV and an energy convergence criterion of 10^{-4} eV . Structural optimization was carried out until the forces acting on each atom fell below $0.005 \text{ eV \AA}^{-1}$.

Data availability

All data generated or analyzed during this study are included in the Article and its Supplementary Information, and are available from the corresponding author upon request.

References

1. *The Sustainable Development Goals (SDGs). The Sustainable Development Goals Report 2022.* (United Nations publication issued by the Department of Economic and Social Affairs, 2022).
2. World Health Organization. *Water Safety Plan Manual. World Health Organization. Water safety plan manual: step-by-step risk management for drinking-water suppliers.* (2023).
3. Ahmed, U., Mumtaz, R., Anwar, H., Mumtaz, S. & Qamar, A. M. Water quality monitoring: from conventional to emerging technologies. *Water Sci. Technol. Water Supply* **20**, 28–45 (2020).
4. Wang, S. et al. Skin electronics from scalable fabrication of an intrinsically stretchable transistor array. *Nature* **555**, 83–88 (2018).
5. Shim, H. et al. An elastic and reconfigurable synaptic transistor based on a stretchable bilayer semiconductor. *Nat. Electron.* **5**, 660–671 (2022).
6. Guan, Y.-S. et al. Elastic electronics based on micromesh-structured rubbery semiconductor films. *Nat. Electron.* **5**, 881–892 (2022).
7. Kwon, K. et al. An on-skin platform for wireless monitoring of flow rate, cumulative loss and temperature of sweat in real time. *Nat. Electron.* **4**, 302–312 (2021).
8. Vikesland, P. J. Nanosensors for water quality monitoring. *Nat. Nanotechnol.* **13**, 651–660 (2018).

9. Brooks, S. M. & Alper, H. S. Applications, challenges, and needs for employing synthetic biology beyond the lab. *Nat. Commun.* **12**, 1–16 (2021).
10. Jung, J. K. et al. Cell-free biosensors for rapid detection of water contaminants. *Nat. Biotechnol.* **38**, 1451–1459 (2020).
11. Atkinson, J. T., Su, L., Zhang, X. & Bennett, G. N. Real-time bioelectronic sensing of environmental contaminants. *Nature* **611**, 548–553 (2022).
12. Terrell, J. L. et al. Bioelectronic control of a microbial community using surface-assembled electrogenetic cells to route signals. *Nat. Nanotechnol.* **16**, 688–697 (2021).
13. Yuk, H., Fuente-Nunez, C. De, Isaacs, F. J. & Zhao, X. Hydrogel-based biocontainment of bacteria for continuous sensing and computation. *Nat. Chem. Biol.* **17**, 724–731 (2021).
14. Petritz, A. et al. Imperceptible energy harvesting device and biomedical sensor based on ultraflexible ferroelectric transducers and organic diodes. *Nat. Commun.* **12**, 2399 (2021).
15. Xu, W. et al. A droplet-based electricity generator with high instantaneous power density. *Nature* **578**, 392–396 (2020).
16. Yin, J. et al. Generating electricity by moving a droplet of ionic liquid along graphene. *Nat. Nanotechnol.* **9**, 378–383 (2014).
17. Zhang, Z. et al. Emerging hydrovoltaic technology. *Nat. Nanotechnol.* **13**, 1109–1119 (2018).
18. Wang, X. et al. Dynamics for droplet-based electricity generators. *Nano Energy* **80**, 105558 (2021).
19. Kim, Y.-J. et al. Walking-induced electrostatic charges enable in situ electroporated disinfection in portable water bottles. *Nat. Water* **2**, 360–369 (2024).
20. Xu, W. & Wang, Z. Fusion of slippery interfaces and transistor-inspired architecture for water kinetic energy harvesting. *Joule* **4**, 2527–2531 (2020).
21. Zi, Y. et al. Standards and figure-of-merits for quantifying the performance of triboelectric nanogenerators. *Nat. Commun.* **6**, 8376 (2015).
22. Belkaid, Y. & Segre, J. A. Dialogue between skin microbiota and immunity. *Science* **346**, 954–959 (2014).
23. Marples, R. R., Downing, D. T. & Kligman, A. M. Control of free fatty acids in human surface lipids by corynebacterium acnes. *J. Invest. Dermatol.* **56**, 127–131 (1971).
24. Jung, Y. H., Park, B., Kim, J. U. & Kim, T. Bioinspired electronics for artificial sensory systems. *Adv. Mater.* **31**, 1803637 (2019).
25. Pan, S. et al. Coatings super-repellent to ultralow surface tension liquids. *Nat. Mater.* **17**, 1040–1047 (2018).
26. Peng, Z., Stingelin, N., Ade, H. & Michels, J. J. A materials physics perspective on structure–processing–function relations in blends of organic semiconductors. *Nat. Rev. Mater.* **8**, 439–455 (2023).
27. Bobrin, V. A. et al. Nano- to macro-scale control of 3D printed materials via polymerization induced microphase separation. *Nat. Commun.* **13**, 3577 (2022).
28. Wong, T. S. et al. Bioinspired self-repairing slippery surfaces with pressure-stable omniphobicity. *Nature* **477**, 443–447 (2011).
29. Nakajima, A., Abe, K., Hashimoto, K. & Watanabe, T. Preparation of hard super-hydrophobic films with visible light transmission. *Thin Solid Films* **376**, 140–143 (2000).
30. Lin, Z. H., Cheng, G., Lee, S., Pradel, K. C. & Wang, Z. L. Harvesting water drop energy by a sequential contact-electrification and electrostatic-induction process. *Adv. Mater.* **26**, 4690–4696 (2014).
31. Won, L. J. et al. Robust nanogenerators based on graft copolymers via control of dielectrics for remarkable output power enhancement. *Sci. Adv.* **3**, e1602902 (2022).
32. Lin, Z. H., Cheng, G., Lin, L., Lee, S. & Wang, Z. L. Water-solid surface contact electrification and its use for harvesting liquid-wave energy. *Angew. Chem. Int. Ed.* **52**, 12545–12549 (2013).
33. Kwak, S. S. et al. Triboelectrification-induced large electric power generation from a single moving droplet on graphene/polytetrafluoroethylene. *ACS Nano* **10**, 7297–7302 (2016).
34. Cao, Y. et al. Self-healing electronic skins for aquatic environments. *Nat. Electron.* **2**, 75–82 (2019).
35. Grimme, S., Antony, J., Ehrlich, S. & Krieg, H. A consistent and accurate ab initio parametrization of density functional dispersion correction (DFT-D) for the 94 elements H–Pu. *J. Chem. Phys.* **132**, 154104 (2010).

Acknowledgements

B.C.K.T. acknowledges support by Agency for Science Technology and Research Singapore (A*STAR) grants A20H8a0241 and M23NBK0090. Y.J.T. acknowledges the funding support from A*Star AME Young Individual Research Grants (AME YIRG), NUS start-up grant, and AM.NUS Fellowship for Young Scientist (FLY). We thank Z. Goh for help with illustrations (Fig. 1a), Dr. Z. Liu, Q. Zhang, X. Fu, Z. Guo, S. Wang, J. Tan, A. Boey, W. Zhang and J. Low for experiment discussion. We thank B. Xiao at the ZEISS Microscopy Customer Center (Shanghai) and Z. Zhang at Carl Zeiss Singapore for assisting in 3D X-ray microscopy (XRM) experiments. We thank Z. Yang for photographs, G. Wan for dielectric constant discussion and T. Shen for EDS mapping test assistance.

Author contributions

B.C.K.T., M.M.L. and H.C.G. conceived and designed the experiments. B.C.K.T. supervised the project. M.M.L., H.C.G., Y.J.T. and K.L.Y. conducted experiments and collected data. H.C.G., K.L.Y. and M.M.L. carried out soft robot experiments. Q.Y.G. and Y.Q.C. performed DFT simulations. E.Z., B.S.T. and M.M.L. conducted AFM and KPFM tests. W.C. and X.Y.W. carried out surface energy calculations. L.L.Z. and H.M.C. synthesized PTFEA polymer. M.M.L., H.C.G., K.L.Y., Y.X.J., X.C. and F.C.L. performed surface morphology characterization. J.Y.Y. performed FTIR measurements. M.M.L., B.C.K.T., H.C.G., H.P.A.A., C.B.H., A.V.Y.T. and Z.L.W. co-wrote the paper. All authors discussed results and commented on the manuscript.

Competing interests

The authors declare no competing interests.

Additional information

Supplementary information The online version contains supplementary material available at <https://doi.org/10.1038/s41467-025-59973-y>.

Correspondence and requests for materials should be addressed to Benjamin C. K. Tee.

Peer review information *Nature Communications* thanks the anonymous, reviewer(s) for their contribution to the peer review of this work. A peer review file is available.

Reprints and permissions information is available at <http://www.nature.com/reprints>

Publisher's note Springer Nature remains neutral with regard to jurisdictional claims in published maps and institutional affiliations.

Open Access This article is licensed under a Creative Commons Attribution-NonCommercial-NoDerivatives 4.0 International License, which permits any non-commercial use, sharing, distribution and reproduction in any medium or format, as long as you give appropriate credit to the original author(s) and the source, provide a link to the Creative Commons licence, and indicate if you modified the licensed material. You do not have permission under this licence to share adapted material derived from this article or parts of it. The images or other third party material in this article are included in the article's Creative Commons licence, unless indicated otherwise in a credit line to the material. If material is not included in the article's Creative Commons licence and your intended use is not permitted by statutory regulation or exceeds the permitted use, you will need to obtain permission directly from the copyright holder. To view a copy of this licence, visit <http://creativecommons.org/licenses/by-nc-nd/4.0/>.

© The Author(s) 2025